Acta Materialia 283 (2025) 120576

Contents lists available at ScienceDirect

Acta Materialia

journal homepage: www.elsevier.com/locate/actamat

Polarization stability and its influence on electrocaloric effects of high entropy perovskite oxide films

Yeongwoo Son [a,*], Stanislav Udovenko [a], Sai Venkata Gayathri Ayyagari [a], John P. Barber [b], Kae Nakamura [a], Christina M. Rost [b], Nasim Alem [a], Susan Trolier-McKinstry [a]

[a] Department of Materials Science and Engineering and Materials Research Institute, The Pennsylvania State University, PA 16802, USA
[b] Department of Materials Science and Engineering, Virginia Polytechnic Institute and State University, Blacksburg, VA 24061, USA

ARTICLE INFO

Keywords:
High entropy perovskite oxides
Thin-film deposition
Electrocaloric effects
Polarization stability
PUND measurement

ABSTRACT

In principle, the configurational entropy inherent in High Entropy Oxides (HEOs) could facilitate large electrocaloric effects (ECE) by promoting polar entropy. In this study, it is demonstrated that the time stability of the remanent polarization can be tuned via B-site disorder in High Entropy Perovskite Oxides (HEPO) films. Eight HEPO powders were synthesized; the propensity for perovskite phase formation was consistent with the Goldschmidt tolerance factor. While entropic contributions stabilize HEPO, they do not fully predict the stabilization. Relative dielectric permittivities between 2000 and 600 can be achieved for the B-site disordered HEPO films with loss tangents below 6 % at room temperature. All films showed similar polarization-electric field loops with maximum polarization up to 48 μC cm^{-2} and a remanent polarization $\geq$ 20 μC cm^{-2} measured at room temperature with applied electric field of 1100 kV cm^{-1} at a frequency of 10 kHz. The temperature of the dielectric maximum (T_{max}) increased from 105 °C to 225 °C with increasing average ion size on the B-site. Polarization stability of the HEPO films was investigated using Positive-Up-Negative-Down (PUND) measurements. It was found that in some HEPO films, 24 % of the remanent polarization decayed within 2 s. By employing the time stability of the remanent polarization, enhanced electrocaloric effects of HEPO film was predicted to be 14.9 K and 11.5 J Kg^{-1} K^{-1} at an applied field of 1120 kV cm^{-1}, for electrocaloric temperature change and entropy change, respectively.

1. Introduction

The electrocaloric effect (ECE) describes the adiabatic temperature change observed in ferroelectric materials originating from the entropy change associated with electric field-induced polarization [1]. Since the discovery of large ECE in 2006, the phenomenon has garnered increased attention as a potential approach for energy-efficient cooling [2]. Thermodynamic simulations suggest that cooling devices utilizing the ECE exhibit superior coefficients of performance relative to mechanical vapor compression coolers, and can achieve a Carnot efficiency exceeding 60 % [3]. Numerous studies have explored electrocaloric materials for the development of advanced cooling devices such as on-chip cooling and battery thermal management systems [4–6]. For this technology to become practical, it will need to enable usefully large adiabatic temperature changes (ΔT), reduced driving electric field (E) to enable adequate cycling reliability, and a broad working temperature range (T_{span}) [7].

Recently, multilayer ceramic capacitor-based electrocaloric prototypes have shown directly measured electrocaloric temperature changes of 5.5 K and a working temperature range of 13 K [8,9]. More specifically, harnessing ferroelectric-to-ferroelectric field induced phase transitions has emerged as a promising approach. Relaxor ferroelectrics are also of interest for ECE applications due to large dipole entropy associated with Nano-Polar Regions (NPRs) [10–14]. Relaxors are typically characterized by short range ordering on one of the cation sites, as has been previously shown in ABO_3 perovskites [15,16]. However, in some cases, the processing of relaxor materials is complicated by relatively poor phase stability, which carries associated difficulties in processing and reproducibility.

The use of configurational entropy to thermodynamically stabilize solid solutions has garnered considerable attention since the discovery of high entropy alloys in 2004 [17,18]. In 2015, $Mg_{0.2}Ni_{0.2}Co_{0.2}Cu_{0.2}Zn_{0.2}O$ was identified as a model rocksalt Entropy-Stabilized Oxide (ESO) [19]. High Entropy Oxide (HEO) is more general term to describe

* Corresponding author.
E-mail address: yxs414@psu.edu (Y. Son).

https://doi.org/10.1016/j.actamat.2024.120576
Received 16 June 2024; Received in revised form 22 October 2024; Accepted 14 November 2024
Available online 17 November 2024

multicomponent systems with near equimolar amounts; ESO, which requires demonstration that a reversible phase transition can be driven by entropy are a subset of HEO [20,21]. Numerous attempts to understand the fundamental properties of these materials and to fabricate new HEOs with different crystal structures have been established. The structural disorder induced by the presence of multiple cations with different sizes and charges on a single lattice site has been shown to benefit various applications as catalysts, capacitors, thermal barriers, batteries, and more. [22–27].

There are four principle influences that high entropy can have on materials, namely high-entropy, lattice distortion, slow diffusion, and cocktail effects [28]. It is speculated that HEO-type materials may enhance the ECE, given that cooperative phenomena such as the polar order inherent to ferroelectricity can be affected by HEO-like formulations, especially through the local structural distortion and the cocktail effect. More specifically, the complex compositions of HEOs are expected to introduce a competition between long-range polar order and local fluctuations due to different atomic sizes and propensities for the displacement from the center of the B-site octahedra. That is, local structural distortion should produce the type of random-bond, random-fields that favor relaxor ferroelectricity relative to normal ferroelectricity [29,30]. This is turn, should favor polar disorder. This can be augmented by a cocktail effect in which some of the ions favor long range polar order, while others do not. While it is known that for ECE, polar entropy plays a pivotal role; nonetheless, the investigation of ECE of HEOs has been rarely reported [31–34].

This paper represents exploratory research on the effect of HEO-like formulations on the ECE and the stability of the induced polarization with time. To do this, the A-sites and B-sites of an ABO_3 perovskite were individually disordered by introducing 5 different elements, while maintaining charge balance and size compatibility. Pb was used as a fixed A-site element for all B-site disordered compositions and Ti was used as a fixed B-site element for all A-site disordered compositions. Overall, eight different compositions were prepared. Table 1 lists the designation and details of each High Entropy Perovskite Oxide (HEPO) composition. Previous work demonstrated that Mn_P was electrically leaky, therefore further investigation was not performed here [34].

2. Experimental procedure

Powder and target preparation: All the investigated compositions were fabricated via conventional solid-state reaction. The raw materials used for this study were acquired from Sigma Aldrich: Pb_3O_4 (99 %), ZrO_2 (99 %), TiO_2 (99.8 %), HfO_2 (98 %), Nb_2O_5 (99.99 %), Al_2O_3 (99.99 %), Fe_2O_3 (99.995 %), Sc_2O_3 (99.9 %), Cr_2O_3 (99.9 %), Na_2CO_3 (99.5 %), Bi_2O_3 (99.999 %), $BaCO_3$ (99.98 %), $SrCO_3$ (99.9 %), $CaCO_3$ (99.9 %), K_2CO_3 (99 %). For the B-site disordered compositions, all the B-site cation precursors were pre-ball-milled with yttria stabilized zirconia media in ethanol for 24 h and heat-treated at 1300 °C for 4 h to homogenize the cation distribution. After adding lead oxide, all the powders were ball-milled again with yttria stabilized zirconia media in ethanol followed by heat treatment at 800 °C for 4 h to achieve a single phase.

A-site disordered compositions were treated in a different way. No pre-treatments were performed for the A-site precursors due to melting. Instead, A-site precursors were mixed with TiO_2 powder and ball-milled with yttria-stabilized zirconia media in ethanol for 24 h. Calcination was performed at 1200 °C for Na_P and K_P and 1050 °C for Pb_P for 4 h, respectively. After the calcination, 20 mol% excess lead oxide, 1 mol% excess sodium, potassium, and bismuth oxide powder were added to the powder batch to compensate for potential loss of those atoms either during for the target processing or during subsequent film growth under vacuum. The powders were vibratory milled with the zirconia media using ethanol for 24 h. Then, the powders were uniaxially pressed into 1-inch in diameter under 0.5 MPa, followed by Cold Isostatic Pressing (CIP) at a pressure of 30 MPa for 1 min. Finally, the pressed ceramic pellets were heat treated at different temperatures from 900 °C to 1300 °C depending on the compositions. All the prepared targets had a relative density ≥94 %.

Deposition of HEPO Films: All deposition of HEPO films was carried out using a custom Pulsed Laser Deposition (PLD) system equipped with 248 nm KrF (102F, Coherent) and (100) $SrRuO_3/SrTiO_3$ crystal substrates (MSE supplies). Prior to the deposition of the $SrRuO_3$ film, a $SrTiO_3$ substrate was chemically etched with buffered-hydrofluoric acid followed by annealing at 1200 °C for 30 min to obtain an atomically smooth surface. A ceramic target of $SrRuO_3$ was purchased from Kojundo, Co, Ltd. Details for the processing parameters and the quality of the $SrRuO_3/SrTiO_3$ are shown in the supplementary material.

All HEPO film depositions were conducted after growth of the $SrRuO_3$ bottom electrode without breaking the vacuum. For the B-site disordered HEPO film, a laser energy of 1.5 J cm^{-2}, a working distance of 6.2 cm, a laser frequency of 6 Hz, an oxygen deposition pressure of 70 mTorr, and a substrate temperature of 595 °C were used. After the deposition, all the films were immediately removed from the heater to avoid loss of volatile species during the cooling process.

Deposition of $PbZr_{0.52}Ti_{0.48}O_3$ film: A commercial solution (PZT-E1, Mitsubishi Materials Corporation, Hyogo, Japan) was used to deposit a PZT film on a Pt-coated SiO_2/Si wafer (NOVA Wafers) by spin coating. The solution was batched with 14 mol% excess Pb, Zr/Ti = 52/48, and 2 % Nb on the B-site. The solution was first dispensed onto the substrate, then spun at 3000 rpm for 45 s, dried at 100 °C for 1 min, pyrolyzed at 400 °C for 4 min, and crystallized in a rapid thermal annealer (RTA) ramping for 40 s from 300 °C to 700 °C with an oxygen partial pressure at 2 standard liters per minute (SLPM). The process was repeated 9 times to achieve a thickness of 770 nm. The processing and quality of the PZT film are described in details elsewhere [35].

Capacitor fabrication: 100 nm thick platinum (Pt) top electrodes were sputter-deposited (CMS-18 sputter system, Kurt J. Lesker Company, Pittsburgh, PA) over the photolithographically-defined double-layer resist stack followed by lift-off. After lift-off, RTA at 500 °C for 15 min was performed in air to promote adhesion between the Pt electrode and the HEPO films.

Structural Characterization: The structural phase and crystallographic orientation of the HEPO powders at room temperature were examined using a PANalytical Empyrean diffractometer with Cu Kα X-ray radiation. Temperature-dependent X-ray diffraction (XRD) data were collected using a PANalytical Empyrean diffractometer and a PANalytical X'Pert Pro MPD equipped with temperature stage HTK 1200 and TTK-450, respectively, both with Cu Kα X-ray radiation, from room temperature to 400 °C. The structural quality of the HEPO films was assessed using a 4-circle high-resolution XRD (Malvern Panalytical-MRD) equipped with a hybrid Ge (220) 2-bounce monochromator and a multilayer mirror for 2Theta and rocking curves or X-ray reflectivity (XRR), respectively, using Cu Kα X-ray radiation. Transmission electron microscopy (TEM) samples were prepared using the FEI Helios 660 Dual Beam Focused Ion Beam (FIB). The FIB lamellae were thinned down at 5 kV followed by 2 kV to reduce FIB induced surface damage. X-ray energy dispersive spectroscopy experiments were performed on the FEI Talos 200X at accelerating voltage of 200 kV. The atomic resolution STEM images were acquired at 300 kV using aberration-corrected Titan G2

Table 1
Designation of 8 different HEPO compositions investigated for this study.

Designation	A-site cations	B-site cations
Al_P	Pb	$(Ti_{0.2}Zr_{0.2}Hf_{0.2}Nb_{0.2}Al_{0.2})$
Cr_P	Pb	$(Ti_{0.2}Zr_{0.2}Hf_{0.2}Nb_{0.2}Cr_{0.2})$
Fe_P	Pb	$(Ti_{0.2}Zr_{0.2}Hf_{0.2}Nb_{0.2}Fe_{0.2})$
Mn_P	Pb	$(Ti_{0.2}Zr_{0.2}Hf_{0.2}Nb_{0.2}Mn_{0.2})$
Sc_P	Pb	$(Ti_{0.2}Zr_{0.2}Hf_{0.2}Nb_{0.2}Sc_{0.2})$
Na_P	$(Bi_{0.2}Ba_{0.2}Sr_{0.2}Ca_{0.2}Na_{0.2})$	Ti
K_P	$(Bi_{0.2}Ba_{0.2}Sr_{0.2}Ca_{0.2}K_{0.2})$	Ti
Pb_P	$(Bi_{0.2}Ba_{0.2}Sr_{0.2}Na_{0.2}Pb_{0.2})$	Ti

microscope. X-ray photoelectron spectroscopy (XPS; Physical Electronics VersaProbe III) were performed using a monochromatic Al Kα X-ray source and a concentric hemispherical analyzer. Charge neutralization was performed using both low energy electrons (<5 eV) and argon ions. The binding energy axis was calibrated using sputter cleaned Cu (Cu $2p_{3/2} = 932.62$ eV, Cu $3p_{3/2} = 75.1$ eV) and Au foils (Au $4f_{7/2} = 83.96$ eV). Peaks were charge referenced to Pb^{2+} band in the Pb 4f spectra at 138.2 eV Measurements were made at a takeoff angle of 90° with respect to the sample surface plane. This resulted in a typical sampling depth of 5–7 nm (95 % of the signal originated from this depth or shallower). Quantification was done using instrumental relative sensitivity factors (RSFs) that account for the x-ray cross section and inelastic mean free path of the electrons. The analysis size was ~200 μm in diameter.

Electrical characterization: The dielectric properties of the films were measured using an HP 4284 LCR meter coupled with a FormFactor 11,000 probe station. An applied voltage 30 mV and a frequency range from 100 Hz to 100 kHz were used. Polarization-Electric field hysteresis loops (P-E loops) were measured using a Precision Multiferroic Tester (Radiant Technologies) using a bipolar triangular waveform. Leakage current densities of the films were measured by 4140 pico-Ampere meter/DC voltage source with a FormFactor 11,000 probe station. Positive-Up-Negative-Down (PUND) measurements were performed using the Precision Multiferroic Tester varying parameters of pulse amplitude (voltage) and delay time. A customized PUND voltage profile was generated using MATLAB and executed using the same tester.

3. Results and discussion

3.1. Structure of high entropy perovskite oxide powders and films

3.1.1. High entropy perovskite oxide powders

As was discussed in the experimental procedure section, depending on the intended stoichiometry, different synthesis strategies were employed for the successful development of the perovskite phase in powders. For the synthesis of the B-site disordered compositions, B-site pre-treatment via a columbite-like route was adapted to discourage formation of the pyrochlore phase during synthesis [36]. It was previously reported that this approach can be applied to HEO-like compositions with compositional disorder on the B-site of the perovskite [34]. With this synthesis method, all B-site HEPO powders were prepared at temperatures ≤ 800 °C. However, the same technique could not be used for the A-site disordered compositions with potassium, sodium, lead, and bismuth, because the precursors melted during pre-treatment steps, even at a temperature of 600 °C. Therefore, the calcination temperature was increased to 1200 °C to stabilize the perovskite phase without homogenizing the A-site powders. The increased temperature compensates for the larger diffusion length required for the non-pre-treated A-site precursors.

Fig. 1(a) shows the XRD patterns of all HEPO powders that formed single perovskite phases. However, despite the pre-treatment steps, Al_P and Cr_P powder were reluctant to form a single phase as shown in Fig. S1 in the supplementary material.

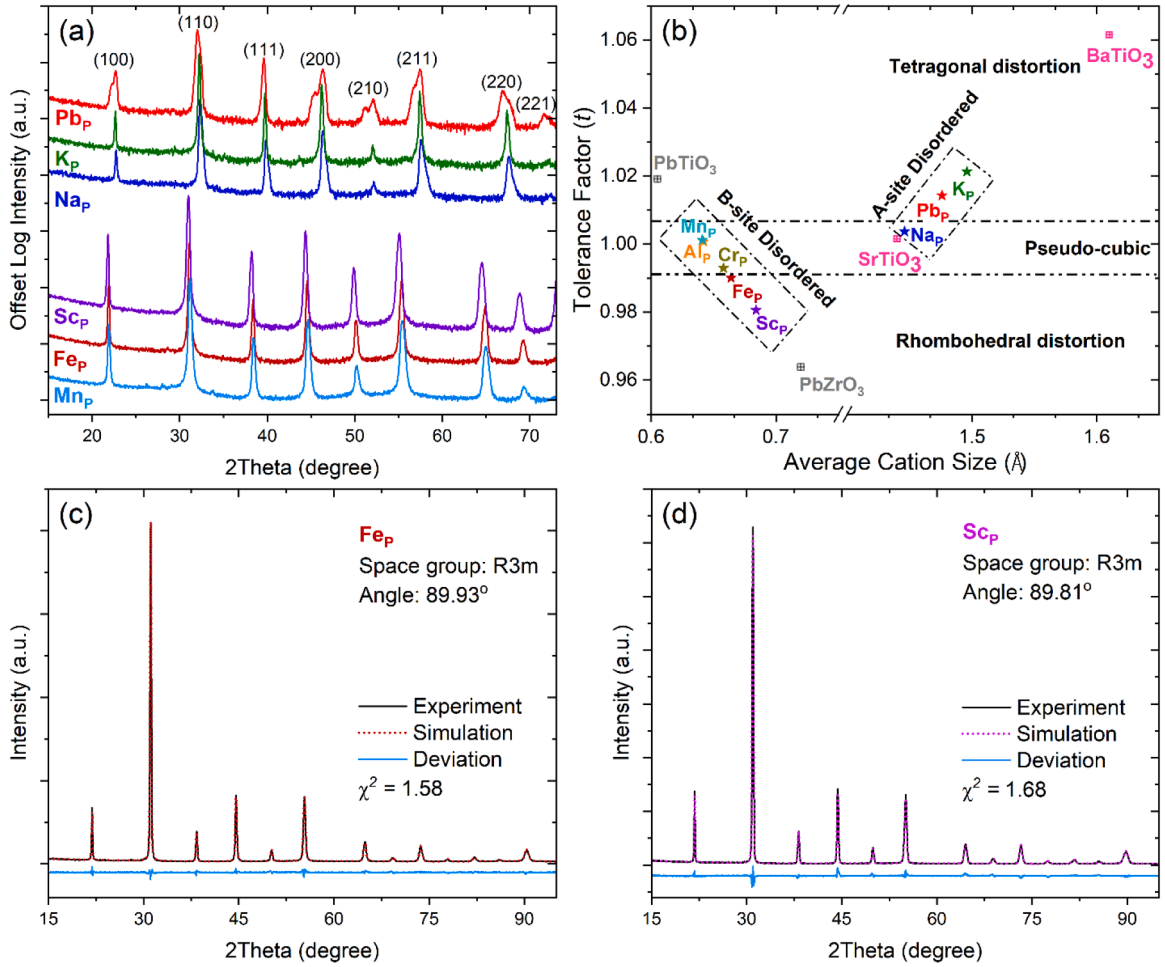

Fig. 1. X-ray diffraction patterns of (a) HEPO powders that form a single perovskite phase, (b) Goldschmidt's tolerance factor versus cation size maps of all HEPO with several well known perovskite materials, (c) Rietveld refinement of Fe_P powder, and (d) Sc_P powder. Refinement revealed rhombohedral distortion with α = 89.93° and 89.81° for the Fe_P and Sc_P powders, respectively.

The lattice parameters of the B-site HEPO powders were larger than those of the A-site HEPOs, which was attributed to the larger averaged B-site cation sizes compared to Ti (0.605 Å) as well as the similar or smaller size of A-site cations than Pb. This also has implications in terms of the stability of the perovskite phase and any anticipated distortions to the perovskite structure, as is expected based on Goldschmidt's tolerance factor [37]. The tolerance factor was calculated via:

$$\text{t (tolerance factor)} = \frac{r_A + r_X}{\sqrt{2}(r_B + r_X)}$$

where r_A is the average radius of the cations on the A-site, r_B is the average radius of the cations on the B-site, and r_X is the radius of the anion [38]; Shannon-Prewitt ionic radii were utilized [38]. Fig. 1(b) presents a map of the tolerance factor as a function of averaged disordered cation size of the eight different HEPO compositions investigated in this study. Several well-known perovskite materials such as $PbTiO_3$, $PbZrO_3$, $SrTiO_3$, and $BaTiO_3$ are shown for comparison.

Table 2 shows the achievability of single phase, the powder lattice parameter, and Goldschmidt's tolerance factor. Previously, it was suggested that HEPO materials with a tolerance factor of $0.97 \leq t \leq 1.03$ are readily prepared as a perovskite single phase [27,39]. This agrees well with the investigation. However, Al_P and Cr_P are exceptions. It is not clear whether the failure to achieve a single phase in Al_P and Cr_P powders is due to either a relatively large enthalpic contribution which exceeds the phase stabilization of the entropic contribution at the processing conditions or to kinetic limitations associated with sluggish diffusion of the given compositions.

Many HEPO compositions had pseudo-cubic-like XRD patterns. However, the doublet in the {200} family peaks for Pb_P suggests a tetragonal distortion. This is consistent with the observation that the perovskite tolerance factor exceeds 1 [40]. Fig. S4(b) shows the result of the temperature dependent XRD for the Pb_P powder; a phase transition from tetragonal to cubic occurred around 250 °C, which is consistent with previous findings [41]. Given this, it is intriguing that K_P with tolerance factor of 1.02 which is larger than that of Pb_P, shows no evidence of the tetragonal structure. It is speculated that this ferroelectric phase transition temperature of K_P is below room temperature, as is the case for $Ba_{0.5}Sr_{0.5}TiO_3$, which has $t = 1.03$ and a phase transition temperature below room temperature [42]. Neither K_P nor Na_P exhibited an obvious phase transition between room temperature and ~ 400 °C, as shown in Fig. S4(a) and (c).

Fe_P and Sc_P powders were rhombohedrally distorted as evidenced by the Rietveld refinement using JADE (as shown in Fig. 1(c) and (d), respectively), and by the splitting of the {222} family peaks in Fig. S2(a) and (b), respectively). Rhombohedral distortion from the cubic cell is quantified in terms of the deviation of the unit cell angles from 90° The larger deviation for Sc_P (89.81°) compared to Fe_P (89.93°), is presumably due to the larger average cation size on the B-site decreasing the tolerance factor. It may also indicate larger displacement of the B site cations from the center of the B-site octahedron [43]. The local tolerance factor accounting for individual B-site cations is shown in Fig. S5. It is clear that the variation in tolerance factor is larger for Al_P composition than for the other B-site disordered compositions. This implies a larger magnitude of lattice distortion in the Al_P composition.

Fig. S3(a) and (b) shows the result of temperature-dependent XRD of the Fe_P and Sc_P powders, respectively, from room temperature to 400 °C. With increasing temperature, the intensity of the {311} and {320} family of perovskite peaks decreased, as the crystal symmetry changed from R3 m to $Pm\bar{3}m$.

3.1.2. High entropy perovskite oxide films

A 45 nm thick layer of $SrRuO_3$ was deposited on (100) $SrTiO_3$ prior to the deposition of any of the B-site HEPO films. Detailed processing information for the SRO/STO is discussed in supplementary material (see Fig. S7). All HEPO films were ~300 nm thick as calibrated by XRR (see Fig. S13(a)). Fig. 2(a), shows an enlarged view of XRD near the {200} perovskite peaks for the B-site disordered HEPO films. A single phase Al_P film was achieved, possibly due to either epitaxial stabilization or to the high effective temperature of the plasma in the PLD process, which increased the entropic contribution (relative to Al_P powder processing). In Fig. S13(b), an AFM scan displays the surface morphology of the B-site disordered HEPO films.

Cr_P did not form a single phase in either a powder or a film. Cr_P films exhibit a large surface roughness, ascribed to $PbCrO_3$ segregation, as seen via XRD (see Fig. S13(c)) and Field Emission Secondary Electron Microscopy (FESEM) with Energy Dispersive Spectroscopy (EDS) mapping (Fig. S13(d)). The surface roughness of the Cr_P film was associated with a well-organized structure aligned along orthogonal directions on the SRO/STO substrate, as seen in the FESEM image. The structure was confirmed to be predominantly $PbCrO_3$ by EDS, which is consistent with the XRD findings.

Fig. 2(c) shows the rocking curves of B-site disordered HEPO films (excepting Cr_P), where the low full width at half maximum, FWHM (<0.061°) demonstrates good film crystallinity. The FWHM of the B-site disordered HEPO films are compared with several well-known relaxor ferroelectric and other HEPO films in Table S1 of the supplementary material. Fig. 2(d) shows the Phi scan for the 101 peaks; a cube-on-cube epitaxial in-plane relationship between the HEPO films and the underlying SRO/STO growth templates can be seen. Table 3 shows the lattice constants, FWHM of the rocking curves and film tetragonalities. In-plane lattice constants were determined via $a = 2\sqrt{(d_{101})^2 - (d_{002})^2}$, where d_{hkl} indicates the lattice spacing corresponding to the given hkl [44]. The difference between the lattice constants for powder and deposited Fe_P and Sc_P films may be due to film stress. It should be noted that all the films are likely to be under compressive in-plane strain, which would increase the out-of-plane lattice constant. In Fig. S15, the asymmetric XRD scan along (101) is shown. It is noteworthy that the in-plane crystallinity exhibits a lower level of crystal perfection compared to its out-of-plane counterpart. This disparity might be attributed to the more sensitive response for edge dislocations along the in-plane direction [45].

The compositional uniformity of the Al_P, Fe_P and Sc_P films were assessed using STEM-EDS as revealed in Fig. S10 – Fig. S12, respectively. We noted that no evident chemical segregation was confirmed at the given length scale. Due to poor reproducibility and large sample-to-sample variation associated with multiple volatile elements in the A-

Table 2
Achievability of single phase (temperature), lattice constant and tolerance factor of the PHEO powders based on XRD.

	Al_P	Cr_P	Fe_P	Mn_P	Sc_P	Na_P	K_P	Pb_P
Single Phase (temp.)	No	No	Yes (800 °C)	Yes (750 °C)	Yes (800 °C)	Yes (1200 °C)	Yes (1200 °C)	Yes (1050 °C)
Lattice constant (Å)	N/A	N/A	4.062 ± 0.002	4.060 ± 0.002	4.078 ± 0.002	3.915 ± 0.002	3.925 ± 0.002	3.913 ± 0.002 (a) 3.989 ± 0.002 (c)
Tolerance factor	1.000	0.993	0.990	1.001	0.981	1.004	1.021	1.014

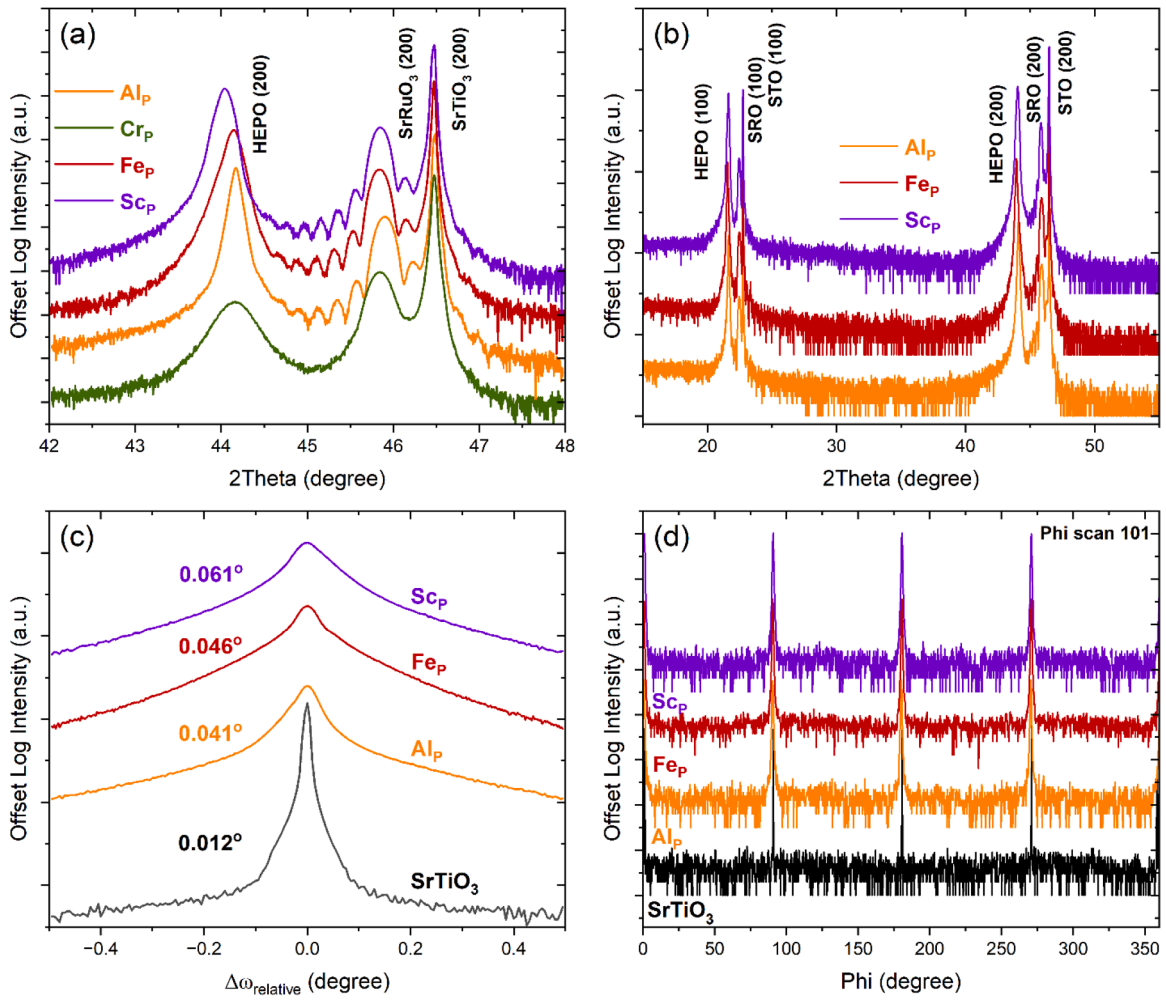

Fig. 2. XRD of the B-site disordered HEPO, (a) enlarged view near (002) family of the perovskite peaks, (b) wider 2theta scan, (c) rocking curve, and (d) phi scan.

Table 3
Lattice constants, FWHM, and tetragonality of the B-site HEPO films determined based on symmetric and asymmetric XRD scans.

	Film Lattice constant (Å)	FWHM (o)	Tetragonality (c/a)
Al$_P$	4.104 ± 0.002 (c) 4.032 ± 0.002 (a)	0.041	1.02
Fe$_P$	4.105 ± 0.002 (c) 4.052 ± 0.002 (a)	0.046	1.01
Sc$_P$	4.109 ± 0.002 (c) 4.065 ± 0.002 (a)	0.061	1.01
Cr$_P$	N/A	N/A	N/A

site disordered film, property exploration was performed on the B-site disordered films only. Details of structure, leakage current, dielectric, and ferroelectric properties of the A-site disordered films at room temperature are given in Fig. S8 of supplementary material.

3.2. Electrical characterizations of the B-site HEPO films

3.2.1. Room-temperature dielectric and ferroelectric properties

Fig. 3(a) – (c) shows room-temperature leakage current density, dielectric permittivity, polarization-electric field hysteresis loops (P-E loop) measurements of the HEPO films, respectively. Leakage current measurements, Fig. 3(a), were made in the field up configuration that caused charge injection from the top Pt electrode. These data were taken with a wait time of 60 s after any change in voltage. It is evident that the Fe$_P$ film had a current density two orders of magnitude higher than the Al$_P$ and Sc$_P$ films. The relatively large leakage of the Fe$_P$ film may be attributed to charge hopping between multivalent Fe-ions, akin to the behavior observed in Mn$_P$ [34]. Indeed, XPS of Fe$_P$ supports the existence of a mixture of Fe^{3+} and Fe^{2+} ions that can induce charge hopping (see Fig. S9). In contrast, Al$_P$ and Sc$_P$ films exhibited relatively little electrical conductivity due to the single valence state of the Al and Sc ions. The dielectric permittivity of the Al$_P$ film was ~2000 with a loss tangent of ~0.05, measured from 100 Hz to 100 kHz, as shown in Fig. 3 (b). Fe$_P$ and Sc$_P$ films showed relatively low dielectric permittivities of ~900 and ~700 with loss tangents of ~0.03 over the measured frequency range. As expected, the Cr$_P$ film displayed a low dielectric permittivity of ~180 with a loss tangent of 0.02, presumably arising from the poor structural properties discussed earlier.

P-E loops of all the B-site disordered films measured at room temperature and 10 kHz are presented in Fig. 3(c). The loops for Al$_P$, Fe$_P$, and Sc$_P$ films share a very similar shape, with Al$_P$ displaying a slightly lower P_{max}, ascribed to the lower propensity for the Al^{3+} to deviate from the center of the octahedron, which would in turn decrease the switchable polarization response [46]. Consistent with the structural and dielectric properties, Cr$_P$ film behaved more like a linear dielectric than a ferroelectric material with a low P_{max} of $\leq 8\ \mu C\ cm^{-2}$.

3.2.2. Temperature-dependent dielectric properties

The temperature-dependent dielectric permittivity and loss tangent for Al$_P$, Fe$_P$, and Sc$_P$ films are shown in Fig. 4(a), (b), and (c), respectively. ΔT_{dis}($= T_{max,100Hz} - T_{max,100KHz}$) was utilized to quantify the degree of dispersion of the dielectric maxima (T_{max}). The Al$_P$ film

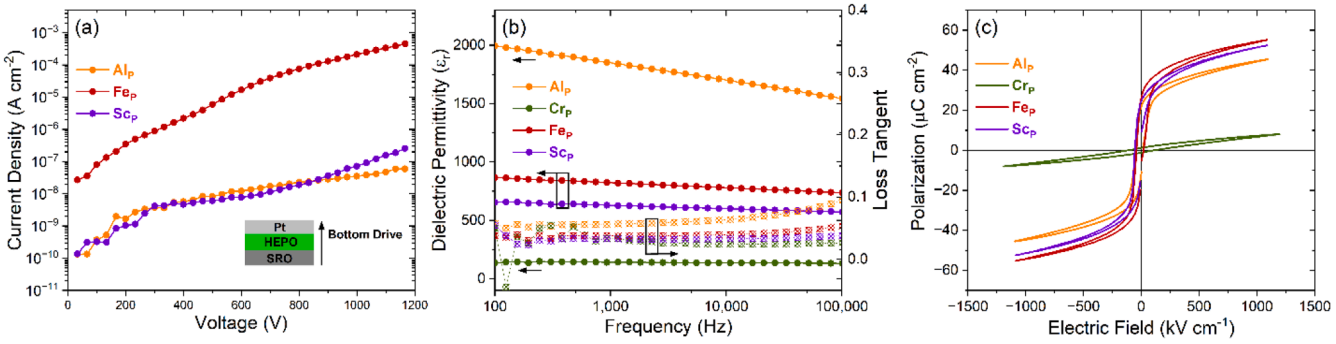

Fig. 3. (a) Current density of the B-site disordered films in response to DC electric fields up to 1300 kV cm^{-1}. The inset shows that the voltage was driven from bottom electrode. (b) Dielectric permittivity and loss tangent of the films measured at room temperature over the frequency range from 100 Hz to 100 kHz. (c) P-E loops of the B-site disordered HEPO films measured at room temperature, 10 kHz, with an applied electric field of 1100 kV cm^{-1}.

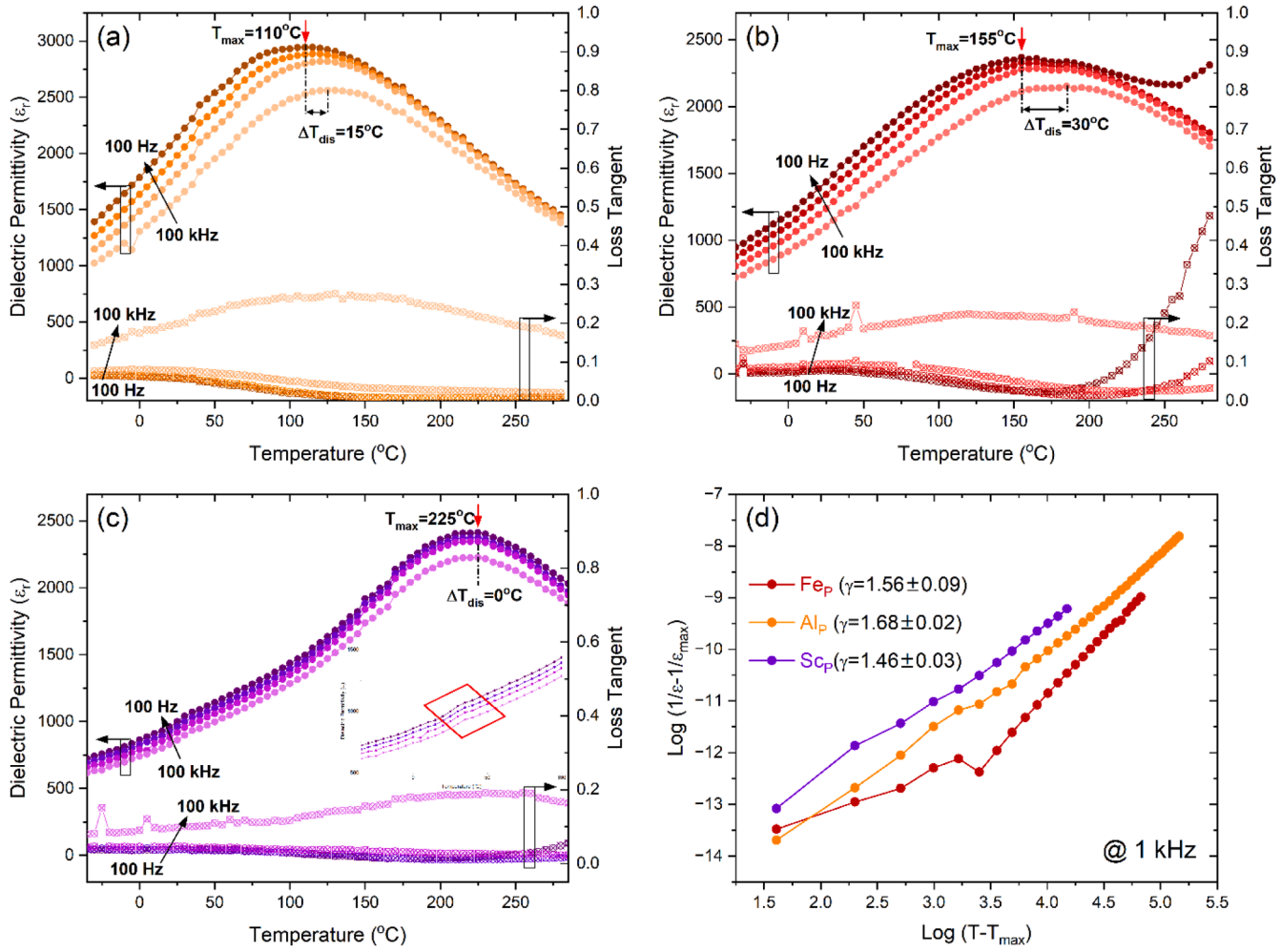

Fig. 4. Temperature-dependent dielectric permittivity and loss tangent of (a) Al_P film, (b) Fe_P film, and (c) Sc_P film. (d) Modified Curie-Weiss law of Al_P, Fe_P, and Sc_P films showing the level of relaxor character (γ).

exhibited strong dispersion of the dielectric permittivity below the T_{max} of 110 °C, with ΔT_{dis} of 15 °C. The dispersion collapses above T_{max}, as is expected in a relaxor ferroelectric. In the Fe_P film (Fig. 4(b)), a higher T_{max} of 155 °C was achieved with a larger ΔT_{dis} of 30 °C. The abrupt increase in the 100 Hz dielectric permittivity and loss tangent above 200 °C, is almost certainly associated with space charge polarizability. Such non-negligible space charge at elevated temperature contributes to the measured dielectric permittivity, resulting in a large ΔT_{dis} of 30 °C [47]. However, interestingly, dielectric dispersion was suppressed for the Sc_P film (ΔT_{dis} of 0 °C). The measured T_{max} was 255 °C, the highest among the B-site disordered HEPO films. This could be linked, at least in part, to the larger rhombohedral distortion in Sc_P, compared to Al_P and Fe_P films. Furthermore, the small hump in the permittivity vs. temperature curve near 35 °C looks like a ferroelectric-ferroelectric transition (possibly a rhombohedral to tetragonal phase transformation), which could provide an additional entropy change for the ECE. Comparing the data for the sample shown, the T_{max} of the HEPO films increased as the average B-site cation size increased.

In Fig. 4(d), the relative degree of relaxation is examined by means of a modified Curie-Weiss law, as shown by:

$$\frac{1}{\varepsilon_r} - \frac{1}{\varepsilon_{max}} = \frac{(T - T_{max})^{\gamma}}{C}$$

where ε_r is the dielectric permittivity, ε_{max} is the maximum dielectric permittivity, C is the Curie-Weiss constant, and γ is the degree of relaxation. In an ideal relaxor ferroelectric, the value of γ is likely to be 2; in an ideal normal ferroelectric, γ is close to 1. The ΔT_{dis} of 0 °C is not always correlated with γ=1.00, as is shown in the case of $K(Ta_{0.55}Nb_{0.45})O_3$ that has γ=1.17, despite a sharp transition [48,49]. Furthermore, the intermediate γ=1.56±0.09 for Fe_P film is very close to that of 0.88Pb$(Zn_{1/3}Nb_{2/3})O_3$–0.12$PbTiO_3$ (γ=1.58) which is between a relaxor and a normal ferroelectric, while γ=1.68±0.02 of Al_P film is very similar to that of $Pb(Mg_{1/3}Nb_{2/3})O_3$ (PMN) (γ=1.70). That is, there is a continuum between relaxor and normal ferroelectric character [50]. Thus, Al_P film behaves more like a relaxor-ferroelectric with γ of 1.68±0.02. Sc_P film behaves more like a normal ferroelectric with γ of 1.46±0.03. In combination with the dielectric permittivity data above, the Sc ion may promote a relatively longer length scale for polar order compared to the other compositions.

3.2.3. *Temperature-dependent ferroelectric properties and electrocaloric effects*

The P-E loops of Al_P, Fe_P, and Sc_P films were measured at 10 kHz from −35 °C to 275 °C. The applied voltage of 32 V (~1100 kV cm^{-1}) was <40 % of the breakdown voltage (~96 V, ~3400 kV cm^{-1}). This was chosen to prevent unintentional sample failure during measurement. The Al_P and Sc_P films maintain slim P-E loops (shown in Fig. S16 (a) and (c)) over the measured temperature range. However, the P-E loops for the Fe_P film become more "banana-like" at high temperatures, due to increasing leakage contributions [51]. These changes were reflected in Fig. 5(a) – (c).

Polarization-Temperature curves (P-T curve) were extracted from the upper branch of the P-E loops. It is clear that the polarization changes in Al_P and Sc_P films from the P-T curve behave similarly. However, bloated "banana-like" P-E loops in the Fe_P film (See Fig. S16 (b)) lead to overestimation of the polarization and misinterpretation of the electrocaloric effects of the material [7,51,52]. From −30 °C to 180 °C, P_{rem} for the Al_P film dropped from 24.7 $\mu C\ cm^{-2}$ to 10.5 $\mu C\ cm^{-2}$, while P_{rem} for Sc_P film decreased from 27.2 $\mu C\ cm^{-2}$ to 13.0 $\mu C\ cm^{-2}$. Interestingly, over this temperature range, P_{rem} of the Al_P film was roughly 85 % that of the Sc_P film. The difference in P_{rem} could be attributed to non-ferroelectrically active Al ion which accounts for 20 % of the B-site cations. To estimate the ECE of the films, an indirect method (based on Maxwell's relations), was employed. This can be expressed as:

$$\Delta T = -\frac{T}{\rho C_p}\int_{E_1}^{E_2}\left(\frac{dP}{dT}\right)_E dE$$

$$\Delta S = \frac{1}{\rho}\int_{E_1}^{E_2}\left(\frac{dP}{dT}\right)_E dE$$

where T is the temperature, ρ is the density of the material, C_p is the specific heat capacity, P is the polarization, and E_1 and E_2 are the initial and final electric fields, respectively. Here, the theoretical density was calculated for each composition; it was assumed that the heat capacity of the films would be comparable to the well-known relaxor ferroelectric, $PbMg_{1/3}Nb_{2/3}O_3 - PbTiO_3$ (PMN-PT) [53]. In Fig. 5(d) – (f), the electrocaloric temperature changes are shown. The Al_P film had a temperature change of 7.39 K at 135 °C for an applied electric field of 1100 kV cm^{-1}. The magnitude of the temperature change was consistent with previous studies, which showed a slightly higher temperature change due to a larger applied field [34]. The other noticeable change was that the maximum electrocaloric temperature change ($T_{max,ECE}$) occurred at higher temperature, compared to the previous study of Al_P on Si that has $T_{max,ECE}$ of 180 °C. Typically, compressive strain shift $T_{max,ECE}$ towards a higher temperature, but the opposite happened here [54]. It is speculated that differences in defect chemistry originating from different

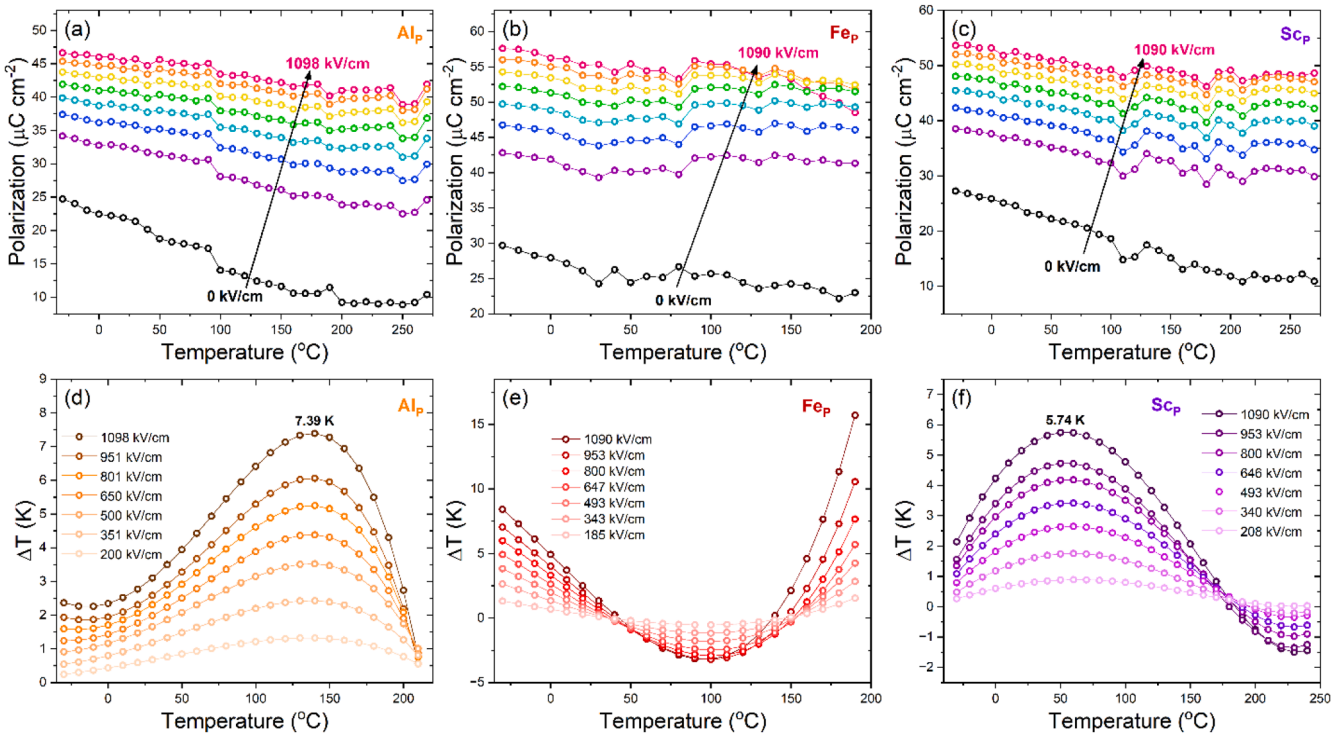

Fig. 5. Polarization as a function of temperature extracted from temperature dependent P-E loops for (a) Al_P film, (b) Fe_P film, and (c) Sc_P film. Indirectly measured electrocaloric temperature change for (d) Al_P film, (e) Fe_P film, and (f) Sc_P film. Data for the Fe_P film are strongly affected by artifacts associated with high field leakage.

growth conditions triggered the change in T_{max}, and ultimately in electrocaloric responses [55].

The appearance of both negative and positive calculated electrocaloric temperature changes for the Fe_P film over the measured temperature range is an artifact associated with high field leakage [56,57].

In spite of the relatively smaller electrocaloric temperature change in the Sc_P film (5.74 K), it had a $T_{max,ECE}$ of 50 °C, close to room temperature [58,59]. The Sc_P film experienced what appears to be a ferroelectric-ferroelectric phase transition measured at low field around 35 °C as shown in Fig. 4(c); this transition temperature could shift with the magnitude of the applied field, and so may be the origin of the electrocaloric temperature peak of 5.74 K near 50 °C. The negative temperature change of Sc_P film above 175 °C is attributed to leakage, as evidenced by a leakage-induced increase in the polarization at ≥ 170 °C (see Fig. S16(c)).

3.3. Polarization stability of the B-site disordered HEPO films

3.3.1. Polarization decay by Positive-up-Negative-down (PUND) measurement

To study the polarization stability of the HEPO films, a voltage pulse was applied as a function of delay time via PUND measurement. A schematic of the PUND waveform can be seen in Fig. 6(a). Briefly, dipoles switched by the first voltage pulse (P^*) are likely to relax over time (pulse delay). The second measurement ($P^\wedge$) captures non-remanent polarization and leakage. This remanent polarization is then $dP = P^* - P^\wedge$. Here, the pulse delay was varied to quantify the dipole relaxation as a function of time. As shown in Fig. 6(b), dP was measured from pulse delays of 1 ms to 100,000 ms with an applied voltage of 32 V for Al_P, Sc_P, and 2 % Nb-doped $PbZr_{0.52}Ti_{0.48}O_3$ (PZT(52/48)) films. The Fe_P film was not included for the polarization stability study due to its leaky response. The magnitude of the change of dP over delay time was calculated via $\Delta dP = dP_{1\ ms} - dP_{100,000\ ms}$. The normal ferroelectric PZT (52/48) film exhibits a small drop in remanent polarization (~1.5 μCcm^{-2}). Likewise, other normal ferroelectrics such as doped-HfO_2, $Al_{0.7}Sc_{0.3}N$, and $BaTiO_3$ films have negligible decay of dP over this time scale [60–62]. In comparison, the polarization drop (ΔdP) for the Sc_P film was 3.2 $\mu C\ cm^{-2}$; in the Al_P film it was 10.3 $\mu C\ cm^{-2}$. It is noted that this significant difference cannot be due to a difference in the structural order, as the Sc_P and Al_P films have very similar FWHM in the X-ray data. Rather, this significant difference suggests that the Al ions break up the long-range polar order, changing the local structural distortions, and causing rapid decay of the dP in the Al_P film (see Fig. S18). Converting this into the frequency domain, 28.0 $\mu C\ cm^{-2}$ of ΔdP can be achieved at 1 kHz, while approximately 21.8 $\mu C\ cm^{-2}$ can be obtained for a 1 Hz cycle, showing the time dependent polarization relaxation of the Al_P film. In contrast, Sc facilitates more long-range polar order, such that a written polarization state is better preserved over time. The difference in polarization relaxation between a normal ferroelectric and a HEPO (or high entropy ferroelectric) is schematically illustrated in Fig. S6. In short, the compositional complexity of the HEPO film frustrates long-range polar ordering, and leads to faster relaxation of the induced polarization. The tendency of the ΔdP in the Al_P film was similar to that reported in $PbZrO_3$, where the switching behavior was perturbed by defect dipoles showing the metastability of remanent dipoles [63].

To further investigate polarization stability in the Al_P and Sc_P films, dP was investigated as a function of applied voltage with varying delay times. A sharp increase of dP in the Sc_P film was observed around 5 V, as highlighted by red arrow in the figure. It is speculated that this is indicative of a field-induced rhombohedral to tetragonal-like phase transition in the Sc_P film given the fact that Sc_P possesses a rhombohedral structure from powder XRD as shown in Fig. 1(d) [64]. This result supports the observation of the ECE peak of the Sc_P film at around 50 °C. Furthermore, development of ferroelectricity in HEO-like formulation is sensitive to specific elements, enabling engineerable ferroelectricity in HEO-like materials.

3.3.2. Estimation of activation energy for depolarization of dipoles

The dP for the Al_P film was measured up to 165 °C, and compared to that of the PZT film. The dP was normalized against $dP_{room\ temperature}$. The temperature-dependent dP was fitted using an Arrhenius-like equation $\ln(\Delta dP) = \exp(-E_a/RT) + \ln(A)$, where E_a is the activation energy for the depolarization with a 10,000 ms delay time, R is the gas constant, T is temperature, and ln(A) is the y-intercept, as shown in Fig. 7(b). The energy required for the depolarization of dipoles in Al_P film is calculated to be ≈87±5 meV while the energy for the PZT film is ≈ 152±2 meV. A 70 nm PZT (25/75) normal ferroelectric capacitor used for ferroelectric memory has been reported to exhibit an activation energy of 280 meV for the depolarization [65]. The comparatively high activation energy for the PZT film is consistent with careful control of the defect chemistry and the quality of the ferroelectric/electrode interfaces essential to ensure retention in the memory. Obviously, the Al_P film has a much smaller activation energy for the depolarization. It is speculated that the large local strain and electric fields created by disorder on the B-site of Al_P film provoke instability of the dipoles, lowering the activation energy for the depolarization.

3.3.3. Enhanced ECE by customized PUND measurement

The polarization decay in Al_P film over time suggests a possible time-dependent enhancement of the ECE. To assess this, PUND data were taken to extract time-dependent P vs T curves. A pulse delay of 2000 ms was chosen. Detailed information of the customized-PUND can be found in the supplementary material (Fig. S19(a) and (b)). The remanent polarization measured via the customized-PUND is shown in Fig. 8(a) – (d) for applied electric fields of 1123 kV cm^{-1}, 807 kV cm^{-1}, 491 kV cm^{-1}, 210 kV cm^{-1}, respectively; the data were fit with a 4th order

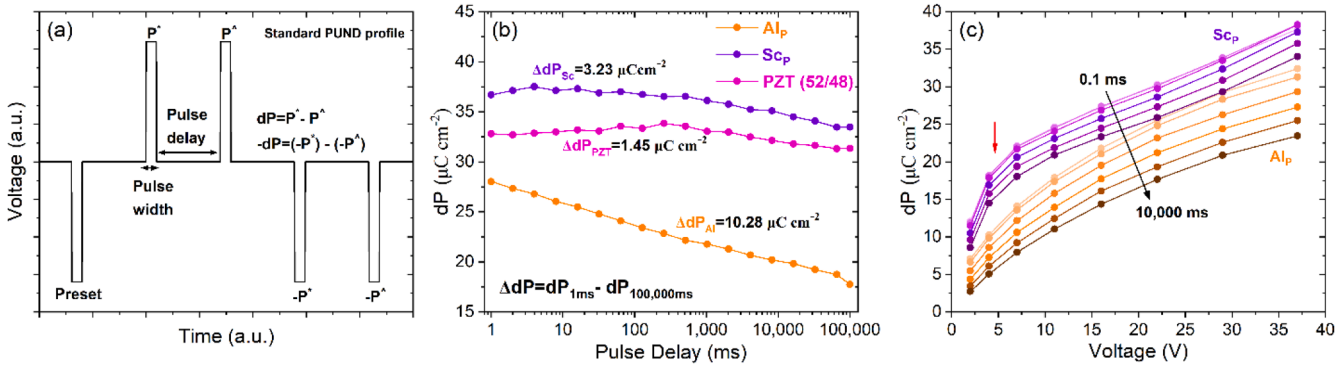

Fig. 6. (a) Schematic of PUND voltage profile. (b) Remanent polarization of Al_P (Orange), PZT (52/48) (Pink) and Sc_P (Purple) films measured by the PUND. (c) Remanent polarization of Al_P and Sc_P films as a function of voltage from 1 V to 37 V for varying pulse delays. The red arrow indicates an abrupt change in dP of Sc_P film which could be associated with field-induced phase transition.

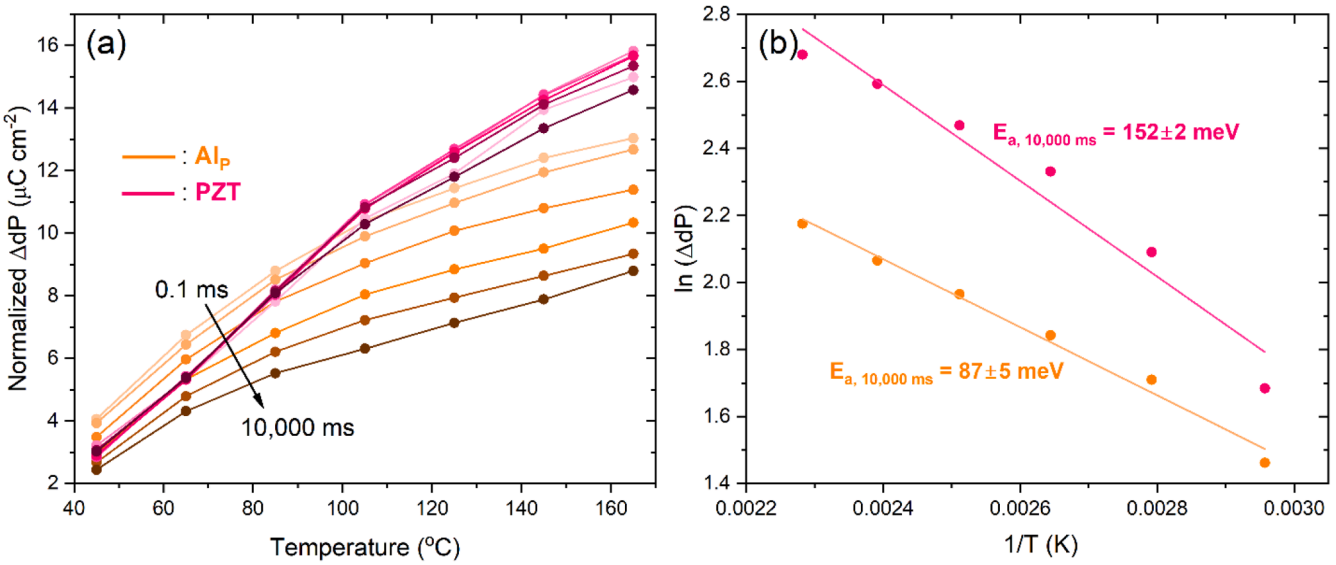

Fig. 7. (a) Normalized remanent polarization of Al_P and PZT films as a function of temperature and (b) activation energy for the depolarization of dipoles estimated by arrhenius equation using dP with 10,000 ms data.

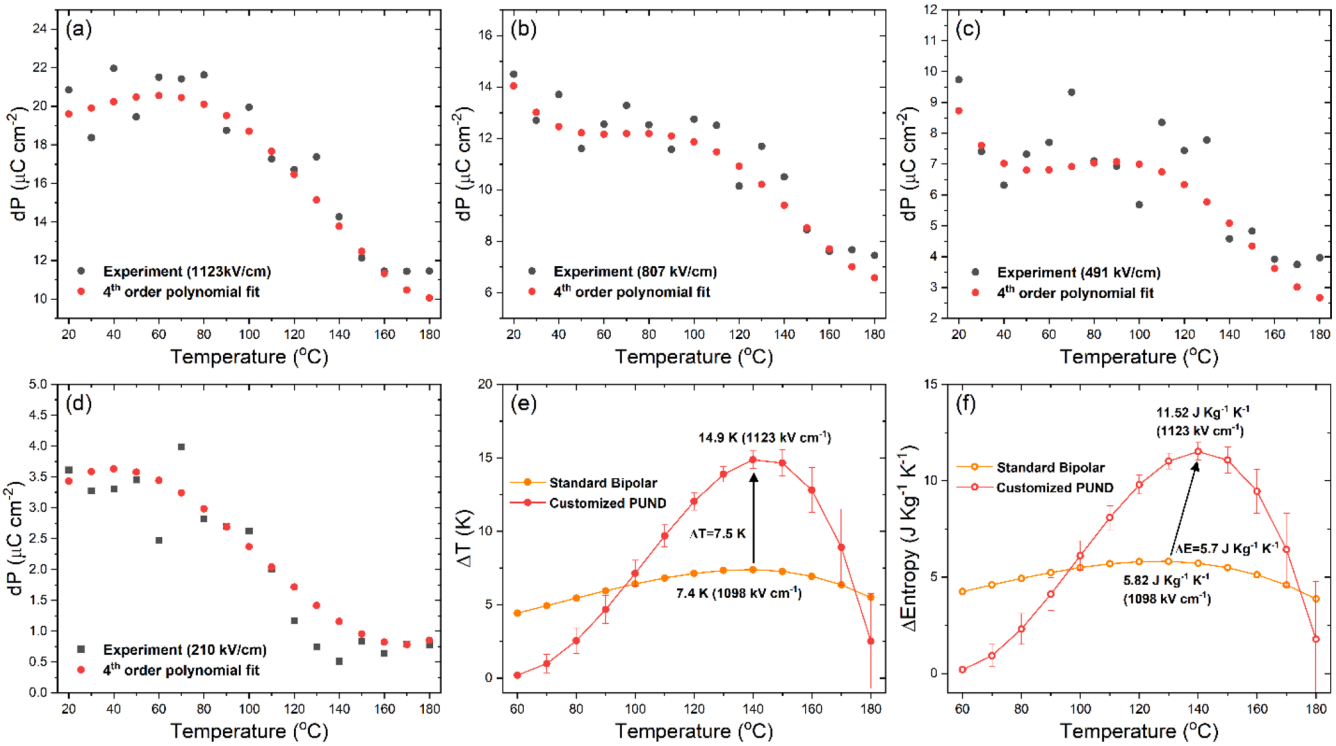

Fig. 8. Remanent polarization (dP) as a function of temperature measured by customized PUND and polynomial fit for applied electric field of (a) 1123 kV cm^{-1}, (b) 807 kV cm^{-1}, (c) 491 kV cm^{-1}, (d) 210 kV cm^{-1}. (e) Enhanced electrocaloric temperature change of Al_P film and (f) entropy change by customized PUND.

polynomial. It was found that a significant polarization drop occurred between 100 °C and 160 °C, as shown in Fig. S20. This range of temperature is consistent with the T_{max} of the Al_P film (110 °C) as well as the peak of ECE measured by standard bipolar P-E loops. However, the time delay boosts relaxation of the polarization. A comparison between standard bipolar P-E loops-induced ECE and the customized PUND-induced ECE is shown in Fig. 8(e) and (f). The electrocaloric temperature and entropy change extracted from the customized-PUND were 14.9 K and 11.52 $J\ Kg^{-1}\ K^{-1}$ respectively, an enhancement of 7.5 K and 7.20 $J\ Kg^{-1}\ K^{-1}$. That is, a delay time of 2000 ms was long enough to randomize dipoles aligned by a voltage pulse so that the polar entropy was markedly enhanced. This ultimately resulted in a larger change in the polarization response, which could double the ECE of the Al_P films. These results provide insights into the development of ferroelectricity in HEO-like materials, including the influence of polarization stability on the functional properties such as ECE.

4. Conclusions

The structural and electrical properties of several different HEPO films were investigated, with an emphasis on the electrocaloric effect and polarization stability. Structural analysis of the HEPO powders

revealed the perovskite tolerance factor controls the ferroelectric distortion observed. HEPO films with disorder on the B-site can be fabricated by pulsed laser deposition with good structural quality on SRO/STO, excepting the Cr_P composition. Fe_P films show high leakage, presumably due to charge hopping. Al_P and Sc_P films displayed relaxor-like and ferroelectric-like behaviors based on dielectric properties, respectively. The electrocaloric temperature change in Al_P and Sc_P films extracted by Maxwell-relations were 7.39 K at 135 °C and 5.74 K at 50 °C, respectively. PUND measurements were employed to study the polarization stability of the films. It showed rapid polarization decay for Al_P films due to the relaxor-like properties associated with the Al ion. A field-induced phase transition for the Sc_P film was observed, which could be a useful source of ECE. The activation energy for the depolarization of the Al_P film was ≈ 87 meV. An enhanced ECE temperature change of 14.9 K was observed for the Al_P film via a customized-PUND that allowed 2000 ms of rest between measurement pulses to promote dipole randomization.

CRediT authorship contribution statement

Yeongwoo Son: Writing – review & editing, Writing – original draft, Visualization, Validation, Methodology, Investigation, Formal analysis, Data curation, Conceptualization. **Stanislav Udovenko:** Visualization, Validation, Software, Investigation. **Sai Venkata Gayathri Ayyagari:** Visualization, Investigation, Data curation. **John P. Barber:** Investigation, Data curation. **Kae Nakamura:** Investigation. **Christina M. Rost:** Supervision, Project administration, Methodology. **Nasim Alem:** Supervision, Project administration, Methodology. **Susan Trolier-McKinstry:** Writing – review & editing, Supervision, Resources, Project administration, Methodology, Investigation, Funding acquisition, Conceptualization.

Declaration of competing interest

The authors declare that they have no known competing financial interests or personal relationships that could have appeared to influence the work reported in this paper.

Acknowledgements

The authors gratefully acknowledge support from the National Science Foundation through the Pennsylvania State University Materials Research Science and Engineering Center DMR-2011839. The authors would also acknowledge Wes Auker for sample preparation for TEM studies.

Supplementary materials

Supplementary material associated with this article can be found, in the online version, at doi:10.1016/j.actamat.2024.120576.

References

[1] S.G. Lu, Q. Zhang, Electrocaloric materials for solid-state refrigeration, Adv. Mater. 21 (2009) 1983–1987.
[2] A. Mischenko, Q. Zhang, J. Scott, R. Whatmore, N. Mathur, Giant electrocaloric effect in thin-film $PbZr_{0.95}Ti_{0.05}O_3$, Science 311 (2006) 1270–1271.
[3] O.V. Pakhomov, S.F. Karmanenko, A.A. Semenov, A.S. Starkov, A.V. Es'kov, Thermodynamic estimation of cooling efficiency using an electrocaloric solid-state line, Tech. Phys. 55 (2010) 1155–1160.
[4] J. Shi, D. Han, Z. Li, L. Yang, S.-G. Lu, Z. Zhong, J. Chen, Q.M. Zhang, X. Qian, Electrocaloric cooling materials and devices for zero-global-warming-potential, high-efficiency refrigeration, Joule 3 (2019) 1200–1225.
[5] R. Ma, Z. Zhang, K. Tong, D. Huber, R. Kornbluh, Y.S. Ju, Q. Pei, Highly efficient electrocaloric cooling with electrostatic actuation, Science 357 (2017) 1130–1134.
[6] H. Gu, X. Qian, X. Li, B. Craven, W. Zhu, A. Cheng, S.C. Yao, Q.M. Zhang, A chip scale electrocaloric effect based cooling device, Appl. Phys. Lett. 102 (2013) 122904. Article.
[7] Y. Sun, S.E. Shirsath, S. Zhang, D. Wang, A reflection on recent efforts in optimization of cooling capacity of electrocaloric thin films, APL Mater 11 (2023) 090602. Article.
[8] A. Torelló, P. Lheritier, T. Usui, Y. Nouchokgwe, M. Gérard, O. Bouton, S. Hirose, E. Defay, Giant temperature span in electrocaloric regenerator, Science 370 (2020) 125–129.
[9] J. Li, A. Torelló, Y. Nouchokgwe, T. Granzow, V. Kovacova, S. Hirose, E. Defay, Electrocaloric effect in $BaTiO_3$ multilayer capacitors with first-order phase transitions, J. Phys. Energy. 5 (2023) 024017. Article.
[10] S.G. Lu, B. Rožič, Q.M. Zhang, Z. Kutnjak, X. Li, E. Furman, L.J. Gorny, M. Lin, B. Malič, M. Kosec, R. Blinc, R. Pirc, Organic and inorganic relaxor ferroelectrics with giant electrocaloric effect, Appl. Phys. Lett. 97 (2010) 162904.
[11] B. Peng, Q. Zhang, B. Gang, G.J.T. Leighton, C. Shaw, S.J. Milne, B. Zou, W. Sun, H. Huang, Z. Wang, Phase-transition induced giant negative electrocaloric effect in a lead-free relaxor ferroelectric thin film, Energy Environ. Sci. 12 (2019) 1708–1717.
[12] A.S. Mischenko, Q. Zhang, R.W. Whatmore, J.F. Scott, N.D. Mathur, Giant electrocaloric effect in the thin film relaxor ferroelectric $0.9Pb\,Mg_{1/3}Nb_{2/3}O_3$-$0.1PbTiO_3$ near room temperature, Appl. Phys. Lett. 89 (2006) 242912. Article.
[13] R. Pirc, Z. Kutnjak, R. Blinc, Q.M. Zhang, Electrocaloric effect in relaxor ferroelectrics, J. Appl. Phys. 110 (2011) 74113. Article.
[14] R.A. Cowley, S.N. Gvasaliya, S.G. Lushnikov, B. Roessli, G.M. Rotaru, Relaxing with relaxors: a review of relaxor ferroelectrics, Adv. Phys. 60 (2011) 229–327.
[15] L.E. Cross, E. Pugh, Relaxor ferroelectrics, Ferroelectrics 76 (1987) 241–267.
[16] C.A. Randall, A.S. Bhalla, T.R. Shrout, L.E. Cross, Classification and consequences of complex lead perovskite ferroelectrics with regard to B-site cation order, J. Mater. Res. 5 (1990) 829–834.
[17] B. Cantor, I.T.H. Chang, P. Knight, A.J.B. Vincent, Microstructural development in equiatomic multicomponent alloys, Mater. Sci. Eng. A. 375–377 (2004) 213–218.
[18] J.W. Yeh, S.K. Chen, S.J. Lin, J.Y. Gan, T.S. Chin, T.T. Shun, C.H. Tsau, S.Y. Chang, Nanostructured high-entropy alloys with multiple principal elements: novel alloy design concepts and outcomes, Adv. Eng. Mater. 6 (2004) 299–303.
[19] C.M. Rost, E. Sachet, T. Borman, A. Moballegh, E.C. Dickey, D. Hou, J.L. Jones, S. Curtarolo, J.-P. Maria, Entropy-stabilized oxides, Nat. Commun. 6 (2015) 1–8.
[20] M. Brahlek, M. Gazda, V. Keppens, A.R. Mazza, S.J. McCormack, A. Mielewczyk-Gryń, B. Musico, K. Page, C.M. Rost, S.B. Sinnott, C. Toher, T.Z. Ward, A. Yamamoto, What is in a name: defining "high entropy" oxides, APL. Mater. 10 (2022) 110902.
[21] S.S. Aamlid, M. Oudah, J. Rottler, A.M. Hallas, Understanding the role of entropy in high entropy oxides, J. Am. Chem. Soc. 145 (2023) 5991–6006.
[22] B. Yang, Y. Zhang, H. Pan, W. Si, Q. Zhang, Z. Shen, Y. Yu, S. Lan, F. Meng, Y. Liu, H. Huang, J. He, L. Gu, S. Zhang, L.Q. Chen, J. Zhu, C.W. Nan, Y.H. Lin, High-entropy enhanced capacitive energy storage, Nat. Mater. 21 (2022) 1074–1080.
[23] F. Li, L. Zhou, J.X. Liu, Y. Liang, G.J. Zhang, High-entropy pyrochlores with low thermal conductivity for thermal barrier coating materials, J. Adv. Ceram. 8 (2019) 576–582.
[24] T.X. Nguyen, Y.-C. Liao, C.-C. Lin, Y.-H. Su, J.-M. Ting, Advanced High Entropy Perovskite Oxide Electrocatalyst for Oxygen Evolution Reaction, Adv. Funct. Mater. 31 (2021) 2101632. Article.
[25] D. Wang, S. Jiang, C. Duan, J. Mao, Y. Dong, K. Dong, Z. Wang, S. Luo, Y. Liu, X. Qi, Spinel-structured high entropy oxide $(FeCoNiCrMn)_3O_4$ as anode towards superior lithium storage performance, J. Alloys Compd. 844 (2020) 156158. Article.
[26] J. Gild, M. Samiee, J.L. Braun, T. Harrington, H. Vega, P.E. Hopkins, K. Vecchio, J. Luo, High-entropy fluorite oxides, J. Eur. Ceram. Soc. 38 (2018) 3578–3584.
[27] S. Jiang, T. Hu, J. Gild, N. Zhou, J. Nie, M. Qin, T. Harrington, K. Vecchio, J. Luo, J. Luo, A new class of high-entropy perovskite oxides, Scr. Mater. 142 (2018) 116–120.
[28] W.L. Hsu, C.W. Tsai, A.C. Yeh, J.W. Yeh, Clarifying the four core effects of high-entropy materials, Nat. Rev. Chem. 8 (2024) 471–485.
[29] R. Blinc, J. Dolinšek, A. Gregorovic, B. Zalar, C. Filipic, Z. Kutnjak, A. Levstik, R. Pirc, Local polarization distribution and edwards-anderson order parameter of relaxor ferroelectrics, Phys. Rev. Lett. 83 (1999) 424–427.
[30] A. Bussmann-Holder, A.R. Bishop, Intrinsic local modes and heterogeneity in Relaxor ferroelectrics, J. Phys.: Condens. Mater. 16 (2004) L313–L320.
[31] W. Liu, F. Li, G. Chen, G. Li, H. Shi, L. Li, Y. Guo, J. Zhai, C. Wang, Comparative study of phase structure, dielectric properties and electrocaloric effect in novel high-entropy ceramics, J. Mater. Sci. 56 (2021) 18417–18429.
[32] Y. Pu, Q. Zhang, R. Li, M. Chen, X. Du, S. Zhou, Dielectric properties and electrocaloric effect of high-entropy $(Na_{0.2}Bi_{0.2}Ba_{0.2}Sr_{0.2}Ca_{0.2})TiO_3$ ceramic, Appl. Phys. Lett. 115 (2019) 0–5.
[33] X. Qian, D. Han, L. Zheng, J. Chen, M. Tyagi, Q. Li, F. Du, S. Zheng, X. Huang, S. Zhang, J. Shi, H. Huang, X. Shi, J. Chen, H. Qin, J. Bernholc, X. Chen, L.-Q. Chen, L. Hong, Q.M. Zhang, High-entropy polymer produces a giant electrocaloric effect at low fields, Nature 600 (2021) 664–669.
[34] Y. Son, W. Zhu, S.E. Trolier-Mckinstry, Electrocaloric effect of perovskite high entropy oxide films, Adv. Electron. Mater. 8 (2022) 220352. Article.
[35] W. Zhu, B. Akkopru-Akgun, J.I. Yang, C. Fragkiadakis, K. Wang, S.W. Ko, P. Mardilovich, S. Trolier-McKinstry, Influence of graded doping on the long-term reliability of Nb-doped lead zirconate titanate films, Acta Mater 219 (2021) 117251. Article.
[36] S.L. Swartz, T.R. Shrout, Fabrication of perovskite lead magnesium niobate, Mater. Res. Bull. 17 (1982) 1245–1250.
[37] H.D. Megaw, Crystal structure of double oxides of the perovskite type, Proc. Phys. Soc. 58 (1946) 133–152.
[38] R.D. Shannon, Revised Effective Ionic Radii and Systematic Studies of Interatomic Distances in Halides and Chalcogenides, Acta. Cryst. Sect. A. 32 (1976) 751–767.

[39] M. Fracchia, M. Coduri, P. Ghigna, U. Anselmi-Tamburini, Phase stability of high entropy oxides: a critical review, J. Eur. Ceram. Soc. 44 (2024) 585–594.
[40] I.M. Reaney, E.L. Colla, N. Setter, Dielectric and structural characteristics of Ba- and Sr-based complex perovskites as a function of tolerance factor, Jpn. J. Appl. Phys. 33 (1994) 3984–3990.
[41] Z. Liu, S. Xu, T. Li, B. Xie, K. Guo, J. Lu, Microstructure and ferroelectric properties of high-entropy perovskite oxides with A-site disorder, Ceram. Int. 47 (2021) 33039–33046.
[42] H.V. Alexandru, C. Berbecaru, A. Ioachim, L. Nedelcu, A. Dutu, BST solid solutions, temperature evolution of the ferroelectric transitions, Appl. Surf. Sci. 253 (2006) 354–357.
[43] M. Ghita, M. Fornari, D.J. Singh, S.V. Halilov, Interplay Between A-site and B-site driven instabilities in perovskites, Phys. Rev. B. 72 (2005) 054114. Article.
[44] M. Zheng, W. Wang, Tunable ferromagnetic transition temperature and vertical hysteretic shift in $SrRuO_3$ films integrated on Si(001), ACS Appl. Mater. Interfaces. 8 (2016) 14012–14018.
[45] Z. Wang, B.H. Goodge, D.J. Baek, M.J. Zachman, X. Huang, X. Bai, C.M. Brooks, H. Paik, A.B. Mei, J.D. Brock, J.P. Maria, L.F. Kourkoutis, D.G. Schlom, Epitaxial $SrTiO_3$ film on silicon with narrow rocking curve despite huge defect density, Phys. Rev. Mater. 3 (2019) 073403. Article.
[46] R.E. Cohen, Origin of ferroelectricity in perovskite oxides, Nature 358 (1992) 136–138.
[47] R.K. Dwivedi, D. Kumar, O. Parkash, Valence compensated perovskite oxide system $Ca_{1-x}La_xTi1-xCr_xO_3$. Part ll: electrical transport behavior, J. Mater. Sci. 36 (2001) 3649–3655.
[48] S. Nomura, K. Uchino, Critical exponents of the dielectric constants in diffused-phase-transition crystals, Ferroelectrics 44 (1982) 55–61.
[49] K. Uchino, Electrostrictive and piezoelectric effects in Relaxor ferroelectrics: historical Background, IEEE Trans. Ultrason. Eng. 69 (2022) 3013–3036.
[50] M.J. Cabral, S. Zhang, E.C. Dickey, J.M. LeBeau, Gradient chemical order in the Relaxor Pb(Mg1/3Nb2/3)O3, 112 (2018), Article 082901.
[51] J.F. Scott, Ferroelectrics Go bananas, J. Phys. Condens. Matter. 20 (2007) 021001. Article.
[52] M. Wu, D. Song, G. Vats, S. Ning, M. Guo, D. Zhang, D. Xue, S.J. Pennycook, X. Lou, Defect-controlled electrocaloric effect in $PbZrO_3$ thin films, J. Mater. Chem. C. Mater. 6 (2018) 10332–10340.
[53] H. Uršič, M. Vrabelj, L. Fulanovič, A. Bradeško, S. Drnovšek, B. Malič, Specific heat capacity and thermal conductivity of the electrocaloric (1-x)$Pb(Mg_{1/3}Nb_{2/3})O_3$–x$PbTiO_3$ ceramics between room temperature and 300°C, J. Microelectron. Electron. Components Mater. 45 (2015) 260–265.
[54] D.L. Shan, C.H. Lei, Y.C. Cai, K. Pan, Y.Y. Liu, Mechanical control of electrocaloric response in epitaxial ferroelectric thin films, Int. J. Solids. Struct. 216 (2021) 59–67.
[55] S. Saremi, J. Kim, A. Ghosh, D. Meyers, L.W. Martin, Defect-Induced (Dis)Order in relaxor ferroelectric thin films, Phys. Rev. Lett. 123 (2019) 207602. Article.
[56] B. Peng, Q. Zhang, Y. Lyu, L. Liu, X. Lou, C. Shaw, H. Huang, Z. Wang, Thermal strain induced large electrocaloric effect of relaxor thin film on $LaNiO_3$/Pt composite electrode with the coexistence of nanoscale antiferroelectric and ferroelectric phases in a broad temperature range, Nano Energy 47 (2018) 285–293.
[57] B. Peng, T. Wang, L. Liu, X. Chen, J. Li, Q. Zhang, R. Yang, W. Sun, Z.L. Wang, P-GaN-substrate sprouted giant pure negative electrocaloric effect in Mn-doped Pb$(Zr_{0.3}Ti_{0.7})O_3$ thin film with a super-broad operational temperature range, Nano Energy 86 (2021) 106059. Article.
[58] J. Hagberg, A. Uusimäki, H. Jantunen, Electrocaloric characteristics in reactive sintered 0.87$Pb(Mg_{1/3}Nb_{2/3})O_3$–0.13$PbTiO_3$, Appl. Phys. Lett. 92 (2008) 132909. Article.
[59] B. Peng, H. Fan, Q. Zhang, A giant electrocaloric effect in nanoscale antiferroelectric and ferroelectric phases coexisting in a relaxor $Pb_{0.8}Ba_{0.2}ZrO_3$ thin film at room temperature, Adv. Funct. Mater. 23 (2013) 2987–2992.
[60] J.W. Adkins, I. Fina, F. Sánchez, S.R. Bakaul, J.T. Abiade, Thermal evolution of ferroelectric behavior in epitaxial $Hf_{0.5}Zr_{0.5}O_2$, Appl. Phys. Lett. 117 (2020) 142902. Article.
[61] R. Nie, S. Shao, Z. Luo, X. Kang, T. Wu, Characterization of ferroelectric $Al_{0.7}Sc_{0.3}N$ thin film on Pt and Mo electrodes, Micromachines (Basel) 13 (2022) 1629. Article.
[62] Y. Jiang, E. Parsonnet, A. Qualls, W. Zhao, S. Susarla, D. Pesquera, A. Dasgupta, M. Acharya, H. Zhang, T. Gosavi, C.C. Lin, D.E. Nikonov, H. Li, I.A. Young, R. Ramesh, L.W. Martin, Enabling ultra-low-voltage switching in $BaTiO_3$, Nat. Mater. 21 (2022) 779–785.
[63] H. Pan, Z. Tian, M. Acharya, X. Huang, P. Kavle, H. Zhang, L. Wu, D. Chen, J. Carroll, R. Scales, C.J.G. Meyers, K. Coleman, B. Hanrahan, J.E. Spanier, L. W. Martin, Defect-induced, ferroelectric-like switching and adjustable dielectric tunability in antiferroelectrics, Adv. Mater. 35 (2023) 2300257. Article.
[64] S.E. Park, T.R. Shrout, Ultrahigh strain and piezoelectric behavior in relaxor based ferroelectric single crystals, J. Appl. Phys. 82 (1997) 1804–1811.
[65] J.A. Rodriguez, K. Remack, K. Boku, K.R. Udayakumar, S. Aggarwal, S. R. Summerfelt, F.G. Celii, S. Martin, L. Hall, K. Taylor, T. Moise, H. McAdams, J. McPherson, R. Bailey, G. Fox, M. Depner, Reliability properties of low-voltage ferroelectric capacitors and memory arrays, IEEE Trans. Device Mater. Reliab. 4 (2004) 436–449.